Chiral limit of nucleon lattice electromagnetic form factors

Walter Wilcox
Department of Physics, Baylor University, Waco, Texas 76798

Terrence Draper and Keh-Fei Liu
Department of Physics, University of Kentucky, Lexington, Kentucky 40506
(Received 1 November 1991)

We calculate electric and magnetic form factors of protons and neutrons in quenched Monte Carlo lattice QCD on a $16^3\times 24$ lattice at $\beta=6.0$ using Wilson fermions. We employ a method which characterizes one of the nucleon fields as a fixed zero-momentum secondary source. Extrapolating the overall data set to the chiral limit, we find acceptable fits for either dipole or monopole forms and extract proton and neutron magnetic moments, the magnitude of which are 10 to 15 % low compared to experiment. In the extrapolation of the dipole fit of the form factors, we find that the dipole-to-nucleon mass ratio is about 7% low compared to experiment. In addition, we obtain positive values of the neutron electric form factor, which, however, are poorly represented by a popular phenomenological form at intermediate to small κ values. A zero-momentum technique for extracting hadron magnetic moments is briefly discussed and shown to yield unrealistically small magnetic moment values.

PACS number(s): 13.40.Fn, 12.38.Gc

I. INTRODUCTION

The techniques of Monte Carlo lattice QCD continue to be developed and applied to numerous quantities of phenomenological interest. In particular, electromagnetic form factors are a useful probe of hadron internal structure. The method used in Ref. [1] characterizes one of the meson interpolating fields as a zero-momentum secondary source. Here, we apply this technique to the nucleon. This allows us, in the final analysis of the quark propagators, to reconstruct a number of operator probes, among which are the various lattice axial-vector and vector currents. We report here on our results using the conserved lattice vector current; see Ref. [2] for preliminary results using an axial probe. Using this technique with separate proton and neutron electric and magnetic sources, we extract all four of the nucleon electromagnetic form factors at any desired lattice momentum transfer. (For an independent implementation of this technique as applied to the proton, see Ref. [3], where, however, only the proton electric form factor is studied.) This investigation for the nucleon is complementary to those in Refs. [4] and [5] which fix the vector current, rather than the particle field, as the secondary source and analyze the full set of spin-$\frac{1}{2}$ baryon form factors, but only for a single momentum-transfer value per quark mass value. See also Ref. [6] for a introduction to the formalism and Ref. [7] for some preliminary results of the present investigation.

The purpose of this study is to begin a comprehensive examination of the mass and momentum dependence of nucleon form factors in the quenched approximation. In our treatment, we will extrapolate the *parameters* of the functional forms rather than individual form factor *values*. This is required if contact with various phenomenological forms for nucleon form factors is to be made.

We begin with an introduction to the formalism of lattice sources and correlation functions. We then present our results for the electric and magnetic form factors and their extrapolation to the chiral limit. We close with a summary and some comments about the directions of future lattice calculations.

II. FORMALISM

A. Fundamentals

In order to set the notation, we first give a fairly complete catalog of the definitions and symbols used in this paper. Our conventions follow Sakurai [8], although we adopt the nonstandard representation γ matrices

$$\{\gamma_\mu,\gamma_\nu\}=2\delta_{\mu,\nu},\quad \gamma_\mu^\dagger=\gamma_\mu\ , \tag{1}$$

$$\gamma=\begin{bmatrix}0 & \sigma\\ \sigma & 0\end{bmatrix},\quad \gamma_4=\begin{bmatrix}I & 0\\ 0 & -I\end{bmatrix},\quad \gamma_5=i\begin{bmatrix}0 & -I\\ I & 0\end{bmatrix}. \tag{2}$$

We use the four-vector notation $b_\mu=(\mathbf{b},ib_0)$, where b_0 is purely real, to ease the transition to Euclidean space. Our discrete Minkowski fermion action is given by

$$S_F^M[\bar\psi,\psi]=-\sum_{I,J}\bar\psi_I M_{IJ}[U^\dagger]\psi_J\ , \tag{3}$$

where $I=\{x,\alpha,a\}$ and $J=\{y,\beta,b\}$, which are in the order {space-time, Dirac, color}. Flavor sums are understood where appropriate. The matrix $M_{IJ}[U^\dagger]$ is defined by

$$M_{IJ}[U^\dagger]\equiv\delta_{I,J}-\kappa\sum_\mu\{(1-\gamma_\mu)_{\alpha\beta}[U_\mu(x)]^{ab}\delta_{x,y-a_\mu}+(1+\gamma_\mu)_{\alpha\beta}[U_\mu^\dagger(x-a_\mu)]^{ab}\delta_{x,y+a_\mu}\}\ . \tag{4}$$

Using $\kappa=1/2(ma+4)$ and (all fields not otherwise specified are lattice fields and a is the lattice spacing)

$$\psi\to\frac{1}{\sqrt{2\kappa}}a^{3/2}\psi^{\rm cont}\ , \tag{5}$$

we find that with $U_\mu^\dagger(x)=e^{iaA_\mu(x)}$, this corresponds to the continuum action

$$S_F^{\rm cont}=-\int d^3x\,dt\times(\bar\psi^{\rm cont}(x)\{\gamma_\mu[\partial_\mu-iA_\mu^{\rm cont}(x)]+m\}\psi^{\rm cont}(x))\ . \tag{6}$$

The assigned $(1\pm\gamma_\mu)$ structure in Eq. (4) means that the upper components of the Dirac equation propagate in the forward-time direction in the static (small-κ) limit. The conserved vector current [9] from Eqs. (3) and (4) is identified from $[\Delta_\mu\omega(x)\equiv\omega(x+a_\mu)-\omega(x)]$

$$\psi(x)\to e^{-i\omega(x)}\psi(x)\ , \tag{7}$$

$$\bar\psi(x)\to\bar\psi(x)e^{i\omega(x)}\ , \tag{8}$$

$$J_\mu\equiv\frac{\delta S_F}{\delta[\Delta_\mu\omega(x)]}\ . \tag{9}$$

$J_\mu=(\mathbf{J},i\rho)$ is given explicitly by (for a single flavor)

$$J_\mu(x)=i\kappa[\bar\psi(x+a_\mu)(1+\gamma_\mu)U_\mu^\dagger(x)\psi(x)-\bar\psi(x)(1-\gamma_\mu)U_\mu(x)\psi(x+a_\mu)]\ . \tag{10}$$

$\rho(x)$ is normalized by $(t>t'>0)$

$$\sum_{\mathbf{x}'}\langle{\rm vac}|\psi_\alpha^a(x)\rho(x')\bar\psi_\beta^b(0)|{\rm vac}\rangle=\langle{\rm vac}|\psi_\alpha^a(x)\bar\psi_\beta^b(0)|{\rm vac}\rangle\ . \tag{11}$$

The interpolating fields we use for the proton are

$$\chi_\alpha(x)=\epsilon^{abc}\psi_\alpha^{(u)a}(x)\psi_\beta^{(u)b}(x)(\tilde C)_{\beta\gamma}\psi_\gamma^{(d)c}(x)\ , \tag{12}$$

$$\bar\chi_{\alpha'}(x)=-\epsilon^{a'b'c'}\bar\psi_{\gamma'}^{(d)c'}(\tilde C)_{\gamma'\beta'}\bar\psi_{\beta'}^{(u)b'}(x)\bar\psi_{\alpha'}^{(u)a'}(x)\ , \tag{13}$$

where $u\leftrightarrow d$ for the neutron. (We assume $m_u=m_d$ throughout.) The charge conjugation matrix $C=\gamma_2$ satisfies $\tilde C\gamma_\mu\tilde C^{-1}=\gamma_\mu^*$, where $\tilde C=C\gamma_5$. We now continue to Euclidean space ($t\to-it$, where t remains real) and use the integration formula [10]

$$\langle{\rm vac}|T(\psi_\alpha(-it_A)\bar\psi_\beta(-it_B)\cdots)|{\rm vac}\rangle=Z^{-1}\int dU\,d\bar\xi\,d\xi\,e^{-S_G^E-S_F^E[\bar\xi,\xi]}\times\xi_\alpha(t_A)\bar\xi(t_B)\cdots\ , \tag{14}$$

where the $\xi,\bar\xi$ are independent, totally anticommuting Grassmann integration variables and S_G^E, $S_F^E[\bar\xi,\xi]$ are the Euclidean gluon, fermion actions [11]. For example, on our lattice (α and β are generic indices)

$$\int d\bar\xi\,d\xi\,\xi_\alpha\bar\xi_\beta e^{-\bar\xi M\xi}=\det(M)S_{\alpha\beta}\ , \tag{15}$$

$$\int d\bar\xi\,d\xi\,\xi_\alpha\bar\xi_\beta\xi_\gamma\bar\xi_\delta e^{-\bar\xi M\xi}=\det(M)(S_{\alpha\beta}S_{\gamma\delta}-S_{\alpha\delta}S_{\gamma\beta})\ , \tag{16}$$

where $S\equiv M^{-1}$.

B. Source technique

For the proton two-point function, we define (assuming $t>0$ in the second line)

$$G_{pp}(t;\mathbf{p},\Gamma)\equiv\sum_{\mathbf{x}}e^{-i\mathbf{p}\cdot\mathbf{x}}\Gamma_{\alpha'\alpha}\langle{\rm vac}|T[\chi_\alpha(x)\chi_{\alpha'}(0)]|{\rm vac}\rangle$$

$$=\sum_{\mathbf{x}}e^{-i\mathbf{p}\cdot\mathbf{x}}\Gamma_{\alpha'\alpha}\epsilon^{abc}(-\epsilon^{a'b'c'})(\tilde C)_{\beta\gamma}(\tilde C)_{\gamma'\beta'}\langle{\rm vac}|\psi_\alpha^{(u)a}(x)\psi_\beta^{(u)b}(x)\psi_\gamma^{(d)c}(x)\bar\psi_{\gamma'}^{(d)c'}(0)\bar\psi_{\beta'}^{(u)b'}(0)\bar\psi_{\alpha'}^{(u)a'}(0)|{\rm vac}\rangle\ . \tag{17}$$

We will specify later the particular Γ matrices which we use here and in following equations. Defining in Dirac space the quantity $\underline{Q}\equiv(\tilde C Q\tilde C^{-1})^T$ for an arbitrary matrix Q, we have [setting $\det(M)=1$]

$$G_{pp}(t;\mathbf{p},\Gamma)=\sum_{\mathbf{x}}e^{-i\mathbf{p}\cdot\mathbf{x}}\epsilon^{abc}\epsilon^{a'b'c'}\{{\rm tr}[\Gamma S^{(u)aa'}(x,0)\underline{S}^{(d)bb'}(x,0)S^{(u)cc'}(x,0)]+{\rm tr}[\Gamma S^{(u)aa'}(x,0)]{\rm tr}[\underline{S}^{(d)bb'}(x,0)S^{(u)cc'}(x,0)]\}\ , \tag{18}$$

where a configuration average is understood and the trace is over Dirac indices only. The corresponding *connected* Wick contractions of the proton three-point function are given as ($\mathbf{q}=\mathbf{p}-\mathbf{p}'$)

$$G_{pJ_\mu p}(t_2,t_1;\mathbf{p},\mathbf{p}',\Gamma)\equiv -i\sum_{\mathbf{x}_2,\mathbf{x}_1} e^{-i\mathbf{p}\cdot\mathbf{x}_2}e^{i\mathbf{q}\cdot\mathbf{x}_1}\Gamma_{\alpha'\alpha}\langle \mathrm{vac}|T[\chi_\alpha(x_2)J_\mu(x_1)\bar{\chi}_{\alpha'}(0)]|\mathrm{vac}\rangle$$

$$=\sum_{\mathbf{x}_2} e^{-i\mathbf{p}\cdot\mathbf{x}_2}\epsilon^{abc}\epsilon^{a'b'c'}\{\mathrm{tr}[\Gamma q_u\hat{S}^{(u)aa'}(x_2,0;t_1,\mathbf{q},\mu)\underline{S}^{(d)bb'}(x_2,0)S^{(u)cc'}(x_2,0)]$$
$$+\mathrm{tr}[\Gamma S^{(u)aa'}(x_2,0)q_d\hat{\underline{S}}^{(d)bb'}(x_2,0;t_1,\mathbf{q},\mu)S^{(u)cc'}(x_2,0)]$$
$$+\mathrm{tr}[\Gamma S^{(u)aa'}(x_2,0)\underline{S}^{(d)bb'}(x_2,0)q_u\hat{S}^{(u)cc'}(x_2,0;t_1,\mathbf{q},\mu)]$$
$$+\mathrm{tr}[\Gamma q_u\hat{S}^{(u)aa'}(x_2,0;t_1,\mathbf{q},\mu)]\mathrm{tr}[\underline{S}^{(d)bb'}(x_2,0)S^{(u)cc'}(x_2,0)]$$
$$+\mathrm{tr}[\Gamma S^{(u)aa'}(x_2,0)]\mathrm{tr}[q_d\hat{\underline{S}}^{(d)bb'}(x_2,0;t_1,\mathbf{q},\mu)S^{(u)cc'}(x_2,0)]$$
$$+\mathrm{tr}[\Gamma S^{(u)aa'}(x_2,0)]\mathrm{tr}[\underline{S}^{(d)bb'}(x_2,0)q_u\hat{S}^{(u)cc'}(x_2,0;t_1,\mathbf{q},\mu)]\}\ . \tag{19}$$

This is similar to the two-point function, except that each quark propagator S has been replaced, in turn, by $q_f\hat{S}$ where q_f is the quark charge ($q_u=\frac{2}{3}$, $q_d=-\frac{1}{3}$) and

$$\hat{S}(x_2,0;t_1,\mathbf{q},\mu)\equiv\kappa\sum_{\mathbf{x}_1} e^{i\mathbf{q}\cdot\mathbf{x}_1}[S(x_2,x_1+a_\mu)(1+\gamma_\mu)U_\mu^\dagger(x_1)S(x_1,0)-S(x_2,x_1)(1-\gamma_\mu)U_\mu(x_1)S(x_1+a_\mu,0)]\ , \tag{20}$$

describes the quark propagator coupled, with momentum $\mathbf{q}$, to the electromagnetic current given in Eq. (10). In order to compactify our notation, let us introduce the quantity

$$[S_A(x_2,0)]^{a'a}_{\alpha'\alpha}\equiv\epsilon^{abc}\epsilon^{a'b'c'}\{[\underline{S}^{bb'}(x_2,0)S^{cc'}(x_2,0)\Gamma]_{\alpha'\alpha}+[\Gamma S^{bb'}(x_2,0)\underline{S}^{cc'}(x_2,0)]_{\alpha'\alpha}$$
$$+\mathrm{tr}[\underline{S}^{bb'}(x_2,0)S^{cc'}(x_2,0)]\Gamma_{\alpha'\alpha}+\mathrm{tr}[\Gamma S^{bb'}(x_2,0)](\underline{S}^{cc'})_{\alpha'\alpha}\}\ , \tag{21}$$

corresponding to the u- (d-) quark contribution to the three-point function for the proton (neutron), as well as

$$[S_B(x_2,0)]^{\alpha'\alpha}_{\alpha'\alpha}\equiv\epsilon^{abc}\epsilon^{a'b'c'}\{[\underline{S}^{bb'}(x_2,0)]\Gamma\underline{S}^{cc'}(x_2,0)]_{\alpha'\alpha}+\mathrm{tr}[\Gamma S^{bb'}(x_2,0)][\underline{S}^{cc'}(x_2,0)]_{\alpha'\alpha}\}\ , \tag{22}$$

corresponding to the d- (u-) quark contribution to the proton (neutron). In addition, define

$$\hat{S}(x_2,0;t_1,\mathbf{q},\mu)\equiv\sum_y S(x_2,y)X(y,0;t_1,\mathbf{q},\mu)\ , \tag{23}$$

where $X(y,0;t_1,\mathbf{q},\mu)$ is given explicitly as

$$X(y,0;t_1,\mathbf{q},\mu)=\kappa\sum_{\mathbf{x}_1} e^{i\mathbf{q}\cdot\mathbf{x}_1}[\delta_{y,x_1+a_\mu}(1+\gamma_\mu)U_\mu^\dagger(x_1)S(x_1,0)-\delta_{y,x_1}(1-\gamma_\mu)U_\mu(x_1)S(x_1+a_\mu,0)]\ . \tag{24}$$

Then we may write concisely, for the proton and neutron,

$$G_{pJ_\mu p}(t_2,t_1;\mathbf{p},\mathbf{p}',\Gamma)=q_u A_{J_\mu}(t_2,t_1;\mathbf{p},\mathbf{p}',\Gamma)+q_d B_{J_\mu}(t_2,t_1;\mathbf{p},\mathbf{p}',\Gamma)\ , \tag{25}$$

$$G_{nJ_\mu n}(t_2,t_1;\mathbf{p},\mathbf{p}',\Gamma)=q_d A_{J_\mu}(t_2,t_1;\mathbf{p},\mathbf{p}',\Gamma)+q_u B_{J_\mu}(t_2,t_1;\mathbf{p},\mathbf{p}',\Gamma)\ , \tag{26}$$

where

$$A_{J_\mu}(t_2,t_1;\mathbf{p},\mathbf{p}',\Gamma)\equiv\sum_{\mathbf{x}_2,y} e^{-i\mathbf{p}\cdot\mathbf{x}_2}\mathrm{Tr}[S_A(x_2,0)S(x_2,y)X(y,0;t_1,\mathbf{q},\mu)]\ , \tag{27}$$

$$B_{J_\mu}(t_2,t_1;\mathbf{p},\mathbf{p}',\Gamma)\equiv\sum_{\mathbf{x}_2,y} e^{-i\mathbf{p}\cdot\mathbf{x}_2}\mathrm{Tr}[S_B(x_2,0)S(x_2,y)X(y,0;t_1,\mathbf{q},\mu)]\ . \tag{28}$$

The Tr notation denotes a trace over both color and Dirac indices.

We have succeeded in rewriting the three-point functions for the proton and the neutron in a very compact manner. However, Eqs. (27) and (28) make it very clear that these quantities cannot be calculated directly because of the presence of the $S(x_2,y)$ propagators, since there are sums over both $\mathbf{x}_2$ and $\mathbf{y}$ present. These equations also make it clear that there are two remedies for this situation. One possibility is to introduce a source to simulate the current, contained in the $X(y,0;t_1,\mathbf{q},\mu)$ factor and associated with the $\mathbf{y}$ sum above. This technique, of course, is not specific to the nucleon and works for any hadron field. However, as one can see from Eq. (24), this choice fixes the spatial momentum transfer $\mathbf{q}$ for a given set of quark propagators. The other possibility is to in-

troduce a source to simulate the two quark lines, contained in S_A and S_B, which lead to the final nucleon associated with the $\mathbf{x}_2$ sum. This technique *is* specific to the nucleon, but leaves the spatial momentum transfer free. Indeed, even the choice of which operator to reconstruct is deferred until the final analysis, so that the propagators calculated are also useful in studying, for example, an axial-vector current. In summary, fixing the current allows one to do a survey of particles with a given probe, whereas fixing the particle source allows one to use a variety of probes on a single particle. We choose here to fix the particle source since we are particularly interested in trying to understand the q^2 dependence of the nucleon form factors.

For this purpose we introduce $v^T_{A,B}(y;t_2,\mathbf{p})$ such that

$$A_{J_\mu}(t_2,t_1;\mathbf{p},\mathbf{p}',\Gamma)=\sum_y \mathrm{Tr}[v^T_A(y;t_2,\mathbf{p})X(y,0;t_1,\mathbf{q},\mu)] , \tag{29}$$

$$B_{J_\mu}(t_2,t_1;\mathbf{p},\mathbf{p}',\Gamma)=\sum_y \mathrm{Tr}[v^T_B(y;t_2,\mathbf{p})X(y,0;t_1,\mathbf{q},\mu)] , \tag{30}$$

where the transpose is over both Dirac and color indices. Explicitly,

$$v^T_{A,B}(y;t_2,\mathbf{p})\equiv\sum_{\mathbf{x}_2} e^{-i\mathbf{p}\cdot\mathbf{x}_2}S_{A,B}(x_2,0)S(x_2,y) . \tag{31}$$

We now multiply on the right of Eq. (31) by $M(y,x')$ and sum on y to give

$$\sum_y v^T_{A,B}(y;t_2,\mathbf{p})M(y,x')=e^{-i\mathbf{p}\cdot\mathbf{x}'}S_{A,B}(x',0) . \tag{32}$$

Using the well-known relation

$$M^\dagger(x,y)=\gamma_5 M(y,x)\gamma_5 , \tag{33}$$

where the dagger works in Dirac and color space, one can show that Eq. (32) leads to

$$\sum_y M(x',y)\gamma_5 v^*_{A,B}(y;t_2,\mathbf{p})=e^{i\mathbf{p}\cdot\mathbf{x}'}\gamma_5 S^\dagger_{A,B}(x',0) . \tag{34}$$

The right-hand side of (34) identifies the sources

$$b_{A,B}(x';t_2,\mathbf{p})\equiv e^{i\mathbf{p}\cdot\mathbf{x}'}\gamma_5 S^\dagger_{A,B}(x',0) , \tag{35}$$

to be inserted in the matrix inverter. Actually, for our purposes, it is more convenient to consider a linear combination of sources,

$$b^{\text{proton}}=q_u b_A+q_d b_B , \tag{36}$$

$$b^{\text{neutron}}=q_d b_A+q_u b_B , \tag{37}$$

which give the desired proton and neutron three-point functions directly. [See Eqs. (25) and (26).]

The general method of using secondary or sequential sources to perform spatial sums over intermediate lattice operators was introduced in Ref. [12].

C. Correlation functions

Although the behavior of Euclidean time nucleon correlation functions on the lattice is standard material [3–7], we summarize their properties for future reference below.

We deal with both protons and neutrons, but for simplicity the following discussion will be for the proton only. The two-point function defined in Eq. (17) in the large Euclidean time limit gives

$$G_{pp}(t;\mathbf{p},\Gamma)\overset{t\gg1}{\rightarrow} N_v\sum_s e^{-Et}\Gamma_{\alpha'\alpha}\langle\mathrm{vac}|\chi_\alpha(0)|\mathbf{p},s\rangle \times\langle\mathbf{p},s|\bar{\chi}_{\alpha'}(0)|\mathrm{vac}\rangle , \tag{38}$$

where N_v is the number of spatial points in the lattice volume. We write lattice and continuum completeness, respectively, for fermionic states as

$$\sum_{n,\mathbf{p},s}|n,\mathbf{p},s\rangle\langle n,\mathbf{p},s|=I , \tag{39}$$

$$\sum_{n,s}\int\frac{d^3p}{(2\pi)^3}\frac{m}{E}|n,\mathbf{p},s)(n,\mathbf{p},s|=I . \tag{40}$$

The continuum limit

$$\frac{1}{V}\sum_{\mathbf{p}}\rightarrow\int\frac{d^3p}{(2\pi)^3} , \tag{41}$$

where $V=N_v a^3$, gives the correspondence between lattice and continuum states

$$|n,\mathbf{p},s\rangle\rightarrow\left[\frac{m}{VE}\right]^{1/2}|n,\mathbf{p},s) . \tag{42}$$

Use of Eqs. (5) and (42) then gives

$$\langle\mathrm{vac}|\chi_\alpha(0)|\mathbf{p},s\rangle\rightarrow\frac{a^3}{(2\kappa)^{3/2}}\left[\frac{m}{N_v E}\right]^{1/2}\times(\mathrm{vac}|\chi^{\mathrm{cont}}_\alpha(0)|\mathbf{p},s) , \tag{43}$$

$$\langle\mathbf{p},s|\bar{\chi}_{\alpha'}(0)|\mathrm{vac}\rangle\rightarrow\frac{a^3}{(2\kappa)^{3/2}}\left[\frac{m}{N_v E}\right]^{1/2}\times(\mathbf{p},s|\bar{\chi}^{\mathrm{cont}}_{\alpha'}(0)|\mathrm{vac}) . \tag{44}$$

$(\mathrm{vac}|\chi^{\mathrm{cont}}_\alpha(0)|\mathbf{p},s)$ and $(\mathbf{p},s|\bar{\chi}^{\mathrm{cont}}_{\alpha'}(0)|\mathrm{vac})$ are related as usual to the free spinors $u_\alpha(\mathbf{p},s)$ and $\bar{u}_{\alpha'}(\mathbf{p},s)$ by

$$(\mathrm{vac}|\chi^{\mathrm{cont}}_\alpha(0)|\mathbf{p},s)=Zu_\alpha(\mathbf{p},s) , \tag{45}$$

$$(\mathbf{p},s|\bar{\chi}^{\mathrm{cont}}_{\alpha'}(0)|\mathrm{vac})=Z^*\bar{u}_{\alpha'}(\mathbf{p},s) , \tag{46}$$

where the unknown amplitude Z transforms as a scalar and therefore cannot depend upon $\mathbf{p}$ or s. Now, using these results in Eq. (38), one obtains

$$G_{pp}(t;\mathbf{p},\Gamma)\overset{t\gg1}{\rightarrow}\frac{|Z|^2a^6}{(2\kappa)^3}\frac{m}{E}e^{-Et}\mathrm{tr}\left[\Gamma\left[\frac{-i\not{p}+m}{2m}\right]\right] , \tag{47}$$

where we have used the following relation for free spinors:

$$\sum_s u(\mathbf{p},s)\bar{u}(\mathbf{p},s)=\frac{-i\not{p}+m}{2m} . \tag{48}$$

For example, with the choice

$$\Gamma_4\equiv\frac{1}{2}\begin{bmatrix} I & 0 \\ 0 & 0 \end{bmatrix} , \tag{49}$$

one obtains

$$G_{pp}(t;\mathbf{p},\Gamma_4)\xrightarrow{t\gg 1}\frac{E+m}{2E}\frac{|Z|^2a^6}{(2\kappa)^3}e^{-Et} . \tag{50}$$

For the proton three-point function, Eq. (19), the large time limit is

$$G_{pJ_\mu p}(t_2,t_1;\mathbf{p},\mathbf{p}',\Gamma)\xrightarrow{(t_2-t_1),t_1\gg 1}-iN_v^2\sum_{s,s'}e^{-E_p(t_2-t_1)}e^{-E_{p'}t_1}\Gamma_{\alpha'\alpha}\langle \mathrm{vac}|\chi_\alpha(0)|\mathbf{p},s\rangle\langle \mathbf{p},s|J_\mu(0)|\mathbf{p}',s'\rangle\langle \mathbf{p}',s'|\bar{\chi}_{\alpha'}(0)|\mathrm{vac}\rangle . \tag{51}$$

The lattice and continuum matrix elements of J_μ are related by

$$\langle \mathbf{p},s|J_\mu(0)|\mathbf{p}',s'\rangle\rightarrow\frac{1}{N_v}\left[\frac{m^2}{E_pE_{p'}}\right]^{1/2}(\mathbf{p},s|J_\mu^{\mathrm{cont}}(0)|\mathbf{p}',s') , \tag{52}$$

where ($\sigma_{\mu\nu}=1/2i[\gamma_\mu,\gamma_\nu]$ and F_1 and F_2 are real)

$$(\mathbf{p},s|J_\mu^{\mathrm{cont}}(0)|\mathbf{p}',s')=i\bar{u}(\mathbf{p},s)\left[\gamma_\mu F_1-\sigma_{\mu\nu}\frac{q_\nu}{2m}F_2\right]u(\mathbf{p}',s') . \tag{53}$$

Based on these forms, with the choices $\mathbf{p}=0$, $\mu=4$, and $\Gamma=\Gamma_4$, the proton three-point function yields

$$G_{pJ_4p}(t_2,t_1;0,-\mathbf{q},\Gamma_4)\xrightarrow{(t_2-t_1),t_1\gg 1}\frac{|Z|^2a^6}{(2\kappa)^3}e^{-m(t_2-t_1)}e^{-Et_1}\left[\frac{E+m}{2E}\right]G_e(q^2) , \tag{54}$$

where $G_e(q^2)\equiv(F_1-[q_\mu^2/(2m)^2]F_2)$ is the electric form factor. Similarly, using

$$\Gamma_k\equiv\frac{1}{2}\begin{bmatrix} \sigma_k & 0 \\ 0 & 0 \end{bmatrix} , \tag{55}$$

one finds that with $\mathbf{p}=0$, $\mu=j$, and $\Gamma=\Gamma_k$

$$G_{pJ_jp}(t_2,t_1;0,-\mathbf{q},\Gamma_k)\xrightarrow{(t_2-t_1),t_1\gg 1}\frac{1}{2E}\frac{|Z|^2a^6}{(2\kappa)^3}e^{-m(t_2-t_1)}e^{-Et_1}\epsilon_{jkl}q_lG_m(q^2) , \tag{56}$$

where $G_m\equiv(F_1+F_2)$ is the magnetic form factor.

Equations (50), (54), and (56) provide the means of calculating G_e and G_m. We do not measure these correlation functions directly, but instead analyze the ratio

$$G_e(q^2)=\left[\frac{2E}{E+m}\right]^{1-t_2/2t'}\times\left[\frac{G_{pJ_4p}(t_2,t_2/2;0,-\mathbf{q},\Gamma_4)}{G_{pp}(t_2;0,\Gamma_4)}\right]\times\left[\frac{G_{pp}(t';0,\Gamma_4)}{G_{pp}(t';\mathbf{q},\Gamma_4)}\right]^{t_2/2t'} , \tag{57}$$

for G_e and

$$G_m(q^2)=\tfrac{1}{2}\epsilon_{jkl}\frac{2E}{q_l}\left[\frac{E+m}{2E}\right]^{t_2/2t'}\times\left[\frac{G_{pJ_jp}(t_2,t_2/2;0,-\mathbf{q},\Gamma_k)}{G_{pp}(t_2;0,\Gamma_4)}\right]\times\left[\frac{G_{pp}(t';0,\Gamma_4)}{G_{pp}(t';\mathbf{q},\Gamma_4)}\right]^{t_2/2t'} , \tag{58}$$

for G_m, which are seen to have smaller error bars. Notice that Eq. (57) guarantees that we measure $G_e(0)=1$ except for convergence errors and that all currents are located halfway between the creation and annihilation time steps. Also notice that the fractional powers are present in order to provide a choice in the two-point functions used in order to allow single exponential behavior to develop in t'. The identities developed in Refs. [1] and [6] show that $G_{pp}(t;\mathbf{q},\Gamma_4)$, $G_{pJ_4p}(t_2,t_1;0,-\mathbf{q},\Gamma_4)$, and $G_{pJ_jp}(t_2,t_1;0,-\mathbf{q},\Gamma_k)$ are real functions in the ensemble average after evenness [Eqs. (50) and (54)] or oddness [Eq. (56)] in spatial momentum $\mathbf{q}$ has been enforced by hand. Because the time interval between the initial and final nucleon sources here is odd, $t_2=15$, we define a *spatial* current operator at half-time steps according to

$$J_j(\mathbf{x}_1,t_1+\tfrac{1}{2})\equiv\tfrac{1}{2}[J_j(\mathbf{x}_1,t_1)+J_j(\mathbf{x}_1,t_1+1)] \tag{59}$$

for use in (56). The time-nonlocal charge density operator J_4 is already naturally associated with half-time steps.

III. RESULTS

Our quenched configurations are $16^3\times 24$ and were calculated using the Monte Carlo Cabibbo-Marinari pseudo heat bath [13]. The SU(3) fundamental Wilson action was used with periodic boundary conditions and $\beta=6.0$. The gauge field was thermalized for 5000 sweeps from a cold start and 12 configurations separated by at least 1000 sweeps were saved. Since our gauge configurations are taken from a single Markov chain, if the resulting correlations between configurations are sufficiently small, then the configurations chosen for analysis are effectively statistically independent. The preferred way to test for autocorrelations is to bin consecutive configurations; we have too few configurations (12) for this to be a useful test. A binning of a larger data set [14] on a quenched lattice at $\beta=6.2$ revealed no evidence of autocorrelations for two-point hadronic functions when configurations were separated by 250–500 (multihit Metropolis) sweeps. An examination of a number of observables as a function of Monte Carlo sweep number in the quenched $\beta=5.9$ form-factor calculation of Ref. [5] revealed no apparent autocorrelations for a sample of 28 configurations separated by 1000 pseudo-heat-bath sweeps. The same sweep-number separation was chosen for calculations of semileptonic form factors in Ref. [15]; we have made this same conservative choice in the present calculation to keep autocorrelations to acceptably low levels.

For the quarks we use periodic boundary conditions in the spatial directions and fixed-time boundary conditions, which consist of setting the quark couplings across the time edge to zero. The origin of all quark propagators was chosen to be at lattice time site 5; the secondary zero-momentum nucleon source was fixed at time site 20. We expect that these positions are sufficiently far from the lattice time boundaries to avoid nonvacuum contaminations. All our results for proton form factors use the point interpolating fields, Eqs. (12) and (13), and similarly for the neutron. We used the conditioned conjugate gradient technique for quark propagator evaluation described in Ref. [16]. For our convergence criterion we demanded that the relative change in the absolute sum of the squares of the quark or secondary propagators be less than 5×10^{-5} over five iterations. As one check of the nucleon secondary source, we verified current conservation for $t_2>t_1>0$ to $\sim 10^{-4}$. Since we wish to calculate the electric and magnetic form factors of both the proton and the neutron, one nonsource and four source propagator inversions are necessary per configuration. The results below include $\kappa=0.154$, 0.152, 0.148, and 0.140. Our statistical error bars come from first- (form factors), second- (form-factor fits), and third-order (chiral extrapolations) single-elimination jackknifes.

We show the pion, ρ, and nucleon masses measured on our 12 configurations in Table I. (The interpolation fields used for the pion and ρ are the usual relativistic ones.) Actually, we show the results of single exponential mass fits using both smeared (over the entire lattice volume using the lattice Coulomb gauge) and point quark propagators. The fits here are for lattice time sites 16–19 for $\kappa=0.154$, 0.152, and 0.148 and time sites 18–21 for $\kappa=0.140$, which was seen to evolve more slowly in time. The smeared and point masses are consistent with one another within the statistical error bars, but a small systematic downward shift of the smeared masses relative to the point masses seems to be present. The smeared results are also consistent with the more accurate $\beta=6.0$ mass results of Ref. [17], with which our largest two κ values overlap. When needed, the smeared mass results from Table I (from our simulation) will be used for the kinematic factors which appear in (57) and (58); the uncertainties associated the kinematics are then included in the form factors as uncorrelated errors, which affects mainly the magnetic error bars. We will also use the accurately determined $\beta=6.0$ value of $\kappa_{\rm cr}=0.157\,08(2)$ from Ref. [18] for our chiral extrapolations. In the following, we will illustrate our data mainly with the $\kappa=0.154$ results, where, it must be kept in mind, the error bars are the worst.

TABLE I. Smeared and point propagator mass fits.

Particle	$\kappa=0.154$	0.152	0.148	0.140
		Smeared case		
π	0.369(9)	0.488(7)	0.677(5)	1.015(5)
ρ	0.46(2)	0.54(1)	0.711(9)	1.032(5)
Nucleon	0.74(4)	0.85(2)	1.12(1)	1.62(1)
		Point case		
κ	0.38(2)	0.49(1)	0.684(9)	1.027(6)
ρ	0.46(2)	0.55(1)	0.721(8)	1.040(7)
Nucleon	0.73(5)	0.87(3)	1.15(2)	1.64(1)
		Ref. [17]		
π	0.361(1)	0.474(1)		
ρ	0.463(3)	0.545(2)		
Nucleon	0.721(7)	0.861(5)		

In order to test for continuum dispersion and to examine the time dependence of our two-point functions, we define the local mass, energy, and energy minus mass from (50) as

$$m(t+\tfrac{1}{2})\equiv\ln\left[\frac{G_{pp}(t;0,\Gamma_4)}{G_{pp}(t+1;0,\Gamma_4)}\right], \tag{60}$$

$$E(t+\tfrac{1}{2})\equiv\ln\left[\frac{G_{pp}(t;\mathbf{p},\Gamma_4)}{G_{pp}(t+1;\mathbf{p},\Gamma_4)}\right], \tag{61}$$

$$[E-m](t+\tfrac{1}{2})\equiv\ln\left[\frac{G_{pp}(t;\mathbf{p},\Gamma_4)G_{pp}(t+1;0,\Gamma_4)}{G_{pp}(t;0,\Gamma_4)G_{pp}(t+1;\mathbf{p},\Gamma_4)}\right]. \tag{62}$$

These quantities are given in Fig. 1 for $\kappa=0.154$ as a function of lattice time. The starting position of all quark propagators is time step 5. The horizontal lines in this figure give the expected result from the continuum dispersion relation using the central value of the measured nucleon mass. The most significant quantity relevant to our form-factor measurements is Eq. (62) since this involves a ratio of quantities that enters in Eqs. (57) and (58). From the figure, it appears that this mea-

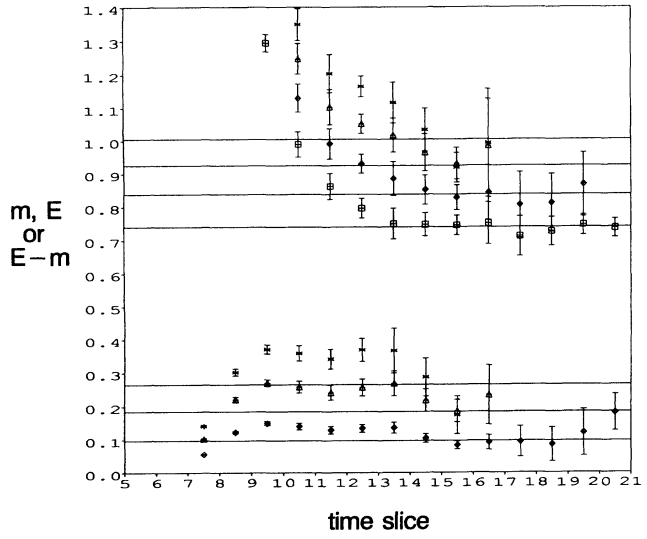

FIG. 1. Local energy, mass, or energy minus mass for the nucleon two-point function, Eqs. (60)–(62) for $\kappa=0.154$ as a function of lattice time slice. In this and the next two figures, the horizontal lines give the expected continuum results based upon the measured mass. All propagators begin at time slice 5.

surement does not become consistent with continuum dispersion until time slice $14\frac{1}{2}$, which corresponds to $t'=9$ in Eqs. (57) and (58). (The propagator time origin is defined to be $t'=0$.) The other κ values are similar, and $t'=9$ is used in all of our form-factor results.

Figures 2 and 3 represent energy minus mass measurements as given by ratios of the three-point functions, Eqs. (54) and (56). These are defined at integer time steps (the currents at t_1 are defined at half-integer sites) by

$$[E-m](t_1+\tfrac{1}{2})|_{j_4}=\ln\left[\frac{G_{pJ_4p}(t_2,t_1;0,-\mathbf{q},\Gamma_4)}{G_{pJ_4p}(t_2,t_1+1;0,-\mathbf{q},\Gamma_4)}\right], \tag{63}$$

$$[E-m](t_1+\tfrac{1}{2})|_{j_k}=\ln\left[\frac{G_{pJ_kp}(t_2,t_1;0,-\mathbf{q},\Gamma_j)}{G_{pJ_kp}(t_2,t_1+1;0,-\mathbf{q},\Gamma_j)}\right]. \tag{64}$$

Figure 2 shows the local $[E-m]$ values from the magnetic three-point function. This function is seen to have a flat exponential behavior that begins quite near the source origin. Figure 3 shows the $[E-m]$ values from the electric three-point function, which, unlike the magnetic case, never appears to flatten. On the other hand, the results *are* consistent with the expected $[E-m]$ values near the midpoint of the lattice where the data for Eqs. (57) and (58) are actually taken.

The results of our form-factor measurements are presented in Tables II–V. Figures 4–7 present the $\kappa=0.154$ graphical results. Notice that the $(qa)^2>0$ values given in the tables are affected very little by the error bars in the nucleon mass (the maximum error bar, at $\kappa=0.154$, is approximately 3% of the central value). Our philosophy in comparing our results to the experiment is to look at the simplest phenomenological forms consistent with the lattice data and then to extrapolate the fit parameters, rather than the individual form-factor values, to the chiral limit. The solid and broken lines in these graphs represent the best *simultaneous* dipole and monopole fits, respectively, of the combined proton electric, magnetic, and neutron magnetic form factors. These are three parameter fits, giving the fit dipole mass from

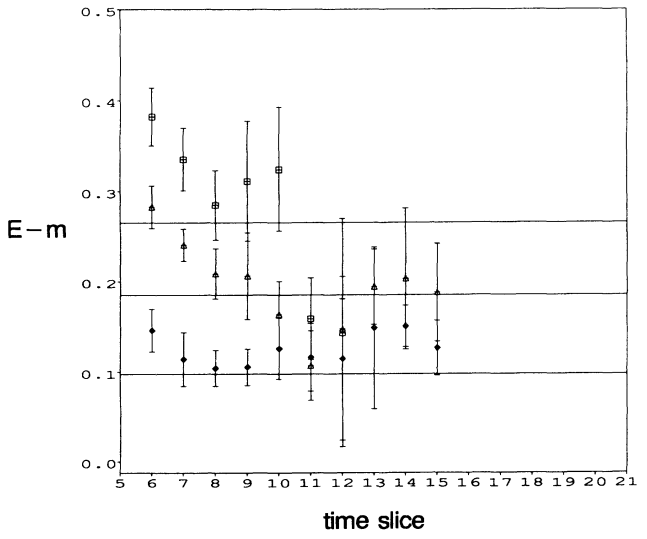

FIG. 2. Local energy mass for the proton magnetic three-point function Eq. (64) at $\kappa=0.154$ as a function of lattice time slice.

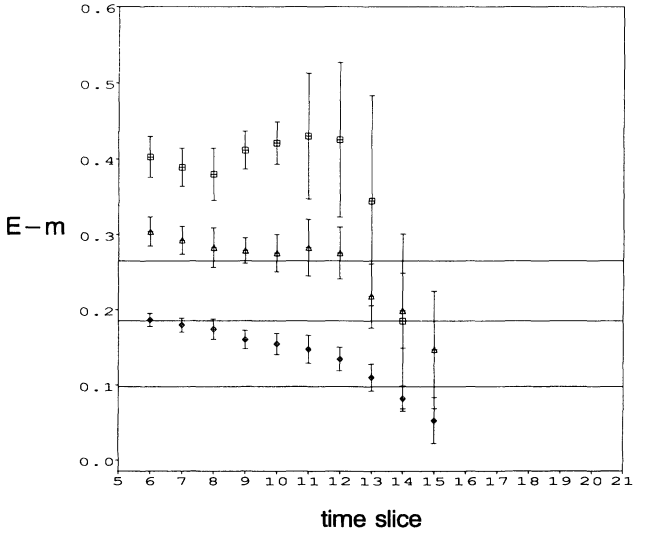

FIG. 3. Local energy minus mass for the proton electric three-point function Eq. (63) at $\kappa=0.154$ as a function of lattice time slice.

TABLE II. Proton and neutron form factors at $\kappa=0.154$ as a function of lattice four-momentum-transfer squared.

Form factor	$(qa)^2=0.145$	0.274	0.392	0.502
G_e^p	0.481(34)	0.335(34)	0.223(34)	0.186(59)
G_m^p	1.17(11)	0.895(90)	0.69(14)	0.86(24)
G_e^n	0.033(17)	0.026(17)	0.046(38)	0.068(67)
G_m^n	−0.748(69)	−0.578(89)	−0.526(88)	−0.54(20)

$$G_e^D(q^2)=\frac{1}{\left[1+q^2/m_D^2\right]^2}\ , \tag{65}$$

or the monopole mass from

$$G_e^M(q^2)=\frac{1}{1+q^2/m_M^2}\ , \tag{66}$$

as well as the proton and neutron magnetic moments from the forms

$$G_m^D(q^2)=\frac{G_m(0)}{\left[1+q^2/m_D^2\right]^2}\ , \tag{67}$$

or

$$G_m^M(q^2)=\frac{G_m(0)}{1+q^2/m_M^2}\ . \tag{68}$$

The fit parameters found this way are listed in Table VI along with the χ^2 per degree of freedom found (χ_d^2), and the dipole/nucleon or monopole/nucleon mass ratio. In general, the quality of the fits are reasonable except for the monopole form at $\kappa=0.140$. The simultaneous monopole fits are seen to be slightly preferable to the dipole ones at the lowest three κ values. Notice also that the ratio m_M/m_N is essentially flat over these three κ values.

In a separate fit of the proton electric form factors, we list in Table VII the dipole and monopole masses, the corresponding charge radii (in lattice units), mass ratios, and χ_d^2 values found. In comparing the χ_d^2 values from the dipole fits in Tables VI and VII, we notice that the inclusion of the magnetic data decreases the quality of the fits at $\kappa=0.154$ and 0.140, whereas it increases the quality at the two intermediate κ values. For the monopole fits, we see that the χ_d^2 values are low in all cases, except again for the $\kappa=0.140$ simultaneous fit. It is the inclusion of the magnetic data that is responsible for the large χ_d^2 value; the values in Table V inform us that the $(qa)^2$ fall-off of the magnetic data is faster than for the proton electric data at this κ value.

Figures 7–10 show the measurements of the neutron electric form factor at the four κ values. The phenomenological form

$$G_e^n(q^2)=-\frac{q^2}{4m_N^2}G_m^n(q^2) \tag{69}$$

is compared to the numerical results, using either the dipole (solid line) or monopole (broken line) parameters from Table VI to characterize $G_m^n(q^2)$. Although the data are quite noisy, we obtain positive values of $G_e^n(q^2)$ in all cases, in agreement with most experiments in this energy regime. In addition, we see that the above phenomenological form fails at the two lowest κ values. This does not rule out such a form in the chiral limit, but does make whatever physics lies behind it less compelling.

Figure 11 shows the $\kappa=0.152$ proton electric form factor. In our measurements we have the option of reconstructing the spatial momentum transfers in a number of different directions for a given $(qa)^2$ value. This figure shows the effect on the error bars of averaging ($\Diamond$) and not averaging ($\Box$) over equivalent momenta. [The $(qa)^2$ values of the nonaveraged data have been increased slightly so that the two data sets do not overlap.] At these values of κ the effect is to reduce the error bars by a factor of 2 to 3.

Also shown in Fig. 11 are the best dipole (solid line) and monopole (broken line) fits to this data from Table VII. These fits illustrate that the source of the large χ_d^2 value seen in the dipole fit of Table VII at $\kappa=0.152$ (and similarly at 0.148) comes about because of the failure of the highest $(qa)^2$ measurement to fall off sufficiently fast. It is possible this is a systematic high $(qa)^2$ lattice artifact; on the other hand, the fact that the $\kappa=0.154$ and 0.140 results do not display similar behavior undercuts this explanation.

Figure 12 represents a comparison of the results of two methods of extracting the proton magnetic moment. In this figure, the data points given by the square symbols

TABLE III. Proton and neutron form factors at $\kappa=0.152$ as a function of lattice four-momentum-transfer squared.

Form factor	$(qa)^2=0.147$	0.281	0.406	0.522
G_e^p	0.551(18)	0.391(24)	0.293(29)	0.288(32)
G_m^p	1.22(7)	0.906(59)	0.696(95)	0.65(13)
G_e^n	0.0230(77)	0.019(11)	0.026(20)	0.038(29)
G_m^n	−0.781(59)	−0.586(47)	−0.474(49)	−0.406(90)

TABLE IV. Proton and neutron form factors at $\kappa=0.148$ as a function of lattice four-momentum-transfer squared.

Form factor	$(qa)^2=0.150$	0.291	0.426	0.555
G_e^p	0.665(10)	0.496(17)	0.390(25)	0.367(27)
G_m^p	1.42(4)	1.03(5)	0.795(66)	0.643(77)
G_e^n	0.0109(31)	0.0116(57)	0.0129(81)	0.016(10)
G_m^n	−0.907(36)	−0.666(32)	−0.520(39)	−0.403(49)

are taken from the dipole fits of Table VI, while the diamond data points are given by the zero-momentum measurement ($t_2>t_1>0$):

$$\frac{\sum_{\mathbf{x}_2,\mathbf{x}_1}\mathrm{tr}[\Gamma_k\langle\mathrm{vac}|\chi(x_2)(x_1)_i J_j(x_1)\bar{\chi}(0)|\mathrm{vac}\rangle]}{\sum_{\mathbf{x}_2}\mathrm{tr}[\Gamma_4\langle\mathrm{vac}|\chi(x_2)\bar{\chi}(0)|\mathrm{vac}\rangle]} = \epsilon_{ijk}\frac{G_m(0)}{2m} . \quad (70)$$

The continuum formula on which the above is based is derived by taking the derivative of the continuum analogue of $G_{pJ_jp}(t_2,t_1;0,-\mathbf{q},\Gamma_k)$ with respect to the ith component of $\mathbf{q}$, evaluated at $\mathbf{q}=0$, and dividing by a zero-momentum two-point function. The resulting equation is then transcribed into lattice language by changing the continuum matrix elements into lattice ones and by making the substitutions $\int d^3x \to a^3\sum_{\mathbf{x}}$ and $J_j^{\mathrm{cont}}(\mathbf{x})\to a^{-3}J_j(\mathbf{x})$. Although the two results agree at the smallest κ, the zero-momentum measurements give unrealistically small magnetic moments at the larger κ values. The reason for this behavior is the same as for similar behavior seen in lattice mesons using charge overlap techniques [19]. Because the lattice matrix elements do not contain arbitrarily small momentum states, the continuum derivative at $\mathbf{q}=0$ cannot be duplicated, and the lattice version would only be expected to hold for $D/2 \gg R$, where D is the length of the lattice on one side and R is a hadron correlation length, say, the charge radius. That is, the hadron is expected to be well contained in the given lattice volume. Apparently, this condition is only beginning to be satisfied at the smallest measured κ value, which is the farthest from the chiral limit.

Figures 13 and 14 represent the chiral extrapolation of the dipole fit proton and neutron magnetic moments. The values found from these fits as well as from similar monopole fits are listed in Table VIII. The quantity $m_q a$ is defined to be

$$m_q a \equiv \frac{1}{2}\left[\frac{1}{\kappa}-\frac{1}{\kappa_{\mathrm{cr}}}\right] . \quad (71)$$

These extrapolations are simply linear fits, which were adequate to describe the data, as seen from the χ_d^2 values. The magnitudes of the magnetic moments are 10 to 15% low; the magnitudes found in Ref. [5] are also low, but by 15 to 30%. There is a hint in these figures that the largest κ values prefer to lie above the linear fit, so more satisfactory magnetic moments may result from a deeper exploration of the region near κ_{cr} where, however, error bars more problematical.

Figure 15 presents the chiral extrapolation of the dipole-to-nucleon mass ratio from Table VIII. This is assumed to be linear as a function of $m_q a$; again, the χ_d^2 values in Tables VIII and IX do not demand a more sophisticated treatment. We prefer to do the chiral extrapolations on the mass *ratios* from the above monopole and dipole fits because the ratio of similar physical quantities is often less subject to systematic errors and because measuring the nucleon mass in relation to other hadrons is best done in a separate high-statistics-spectrum calculation, such as the $\beta=6.0$ calculations of Refs. [17] and [18]. For comparison, we have provided the results of three-parameter (Table VIII) and one-parameter (Table IX) fits of experimental nucleon data taken from Refs. [20] and [21]. Setting the scale from the chiral limit nucleon mass of Ref. [18], our four-momentum-transfer range roughly corresponds to $0.6\ \mathrm{GeV}^2 \le q^2 \le 1.9\ \mathrm{GeV}^2$; the values overlapping with this range from these references are the values used in the fits, which are listed in Tables X and XI. The χ_d^2 values for the experimental results, which are more precise than the lattice measurements, show that more parameters are really required in this energy range to produce reasonable phenomenological fits. We have $\chi_d^2=1.99$ and 10.7 for the dipole and monopole fits, respectively, of the proton electric data in Table IX. Similarly, we obtain $\chi_d^2=3.39$ and 35.5 for the dipole and monopole fits, respectively, of Table VIII. In

TABLE V. Proton and neutron form factors at $\kappa=0.140$ as a function of lattice four-momentum-transfer squared.

Form factor	$(qa)^2=0.152$	0.300	0.444	0.584
G_e^p	0.791(8)	0.646(14)	0.539(18)	0.484(21)
G_m^p	1.44(3)	1.12(3)	0.895(41)	0.740(37)
G_e^n	0.0030(10)	0.0043(16)	0.0048(22)	0.041(28)
G_m^n	−0.927(22)	−0.726(25)	−0.582(30)	−0.476(22)

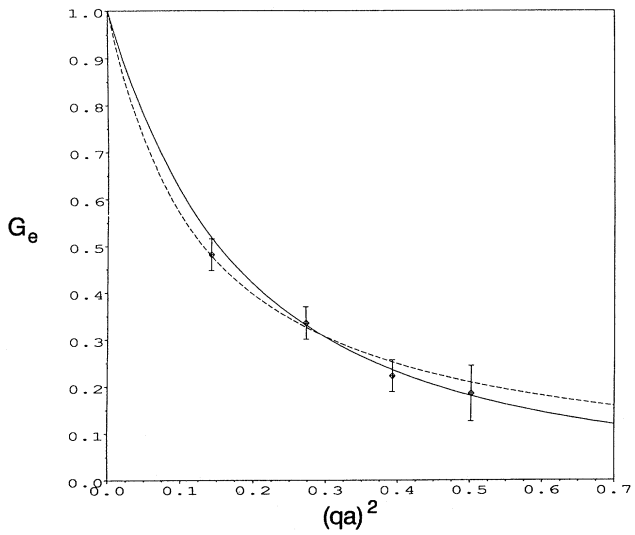

FIG. 4. Electric form factor of the proton at $\kappa=0.154$ as a function of lattice Minkowski four-momentum-transfer squared. The solid and broken lines represent the best *simultaneous* dipole and monopole fits, respectively, of the proton electric, magnetic, and neutron magnetic form factors. The parameters of the fits are listed in Table VI.

comparing the two experimental fits, we notice that the dipole mass ratio is slightly larger when the magnetic data is included (Table VIII) than when it is not (Table IX). Experiment shows that the proton and neutron magnetic form factors fall off significantly more slowly than the proton electric form factor in our energy regime [22]. This explains the tendency of the experimental dipole fit which includes the magnetic data, to produce a larger value of m_D/m_N than a similar fit of the proton electric data alone. It is encouraging that the same tendency seems to be present in the lattice dipole results in Tables VIII and IX, although the overall value for the ratio seems to be about 7% low in either case. However, as in the magnetic moment case, the larger κ values of this ratio prefer to lie above the linear fit, and therefore a more satisfactory value of this ratio could result from a deeper exploration of the chiral limit.

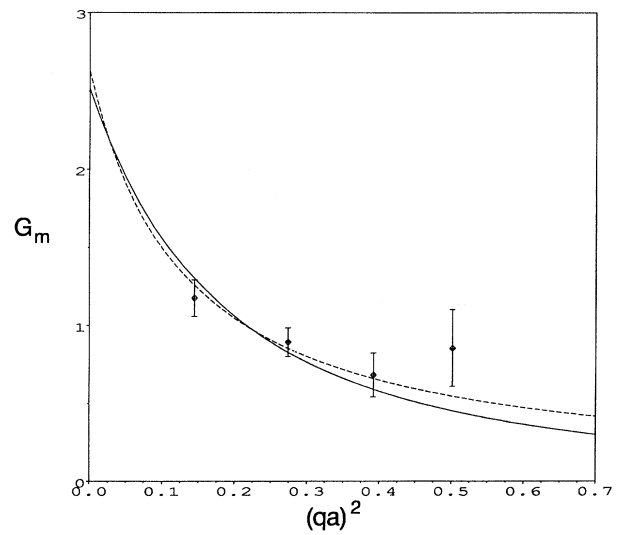

FIG. 5. Magnetic form factor of the proton at $\kappa=0.154$ as a function of lattice Minkowski four-momentum-transfer squared. The solid and broken lines are simultaneous dipole and monopole fits, respectively, as explained in the Fig. 4 caption.

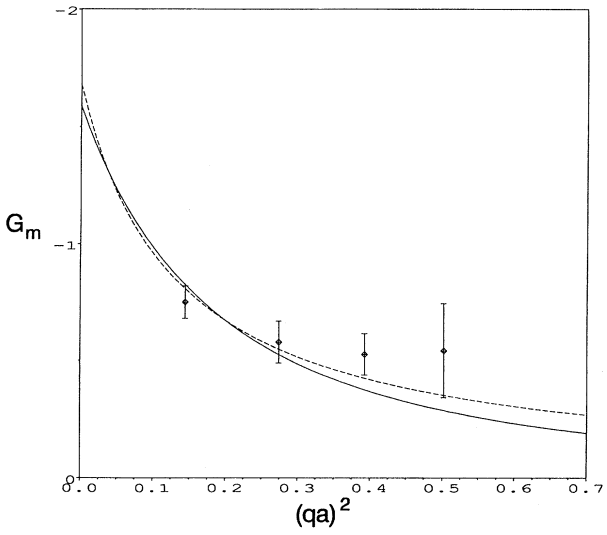

FIG. 6. Magnetic form factor of the neutron at $\kappa=0.154$ as a function of lattice Minkowski four-momentum-transfer squared. The solid and broken lines are simultaneous dipole and monopole fits, respectively, as explained in the caption to Fig. 4.

IV. COMPARISON AND CONCLUSIONS

We have investigated the functional forms of the nucleon electromagnetic form factors as given by quenched lattice QCD. Although our results are not sufficiently accurate to distinguish between monopole and dipole fits to the data, we have seen that the error bars on these quan-

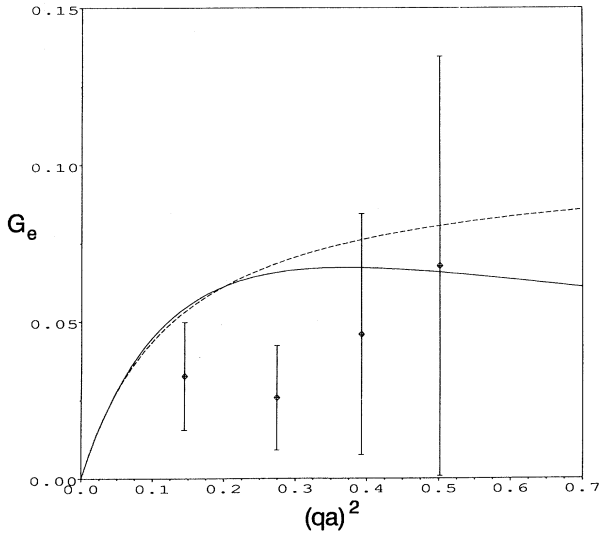

FIG. 7. Electric form factor of the neutron at $\kappa=0.154$ as a function of lattice Minkowski four-momentum-transfer squared. The lines shown represent the phenomenological form Eq. (69) using either dipole (solid line) or monopole (broken line) fits of the neutron magnetic form factor from Table VI.

TABLE VI. Combined dipole and monopole fits of the proton electric and magnetic, neutron magnetic form factors.

		$\kappa=0.154$	0.152	0.148	0.140
Dipole	$m_D a$	0.609(31)	0.688(21)	0.832(18)	1.09(3)
	m_D/m_N	0.823(61)	0.809(31)	0.743(17)	0.675(19)
	$G_m^p(0)$	2.51(18)	2.22(10)	2.09(6)	1.77(5)
	$G_m^n(0)$	−1.59(13)	−1.45(10)	−1.34(5)	−1.14(4)
	χ_d^2	1.36	1.45	0.66	1.63
Monopole	$m_M a$	0.364(31)	0.427(19)	0.539(16)	0.725(24)
	m_M/m_N	0.492(49)	0.503(26)	0.481(15)	0.447(15)
	$G_m^p(0)$	2.63(22)	2.26(10)	2.09(6)	1.77(6)
	$G_m^n(0)$	−1.68(18)	−1.46(11)	−1.33(5)	−1.13(5)
	χ_d^2	0.70	0.25	0.64	3.57

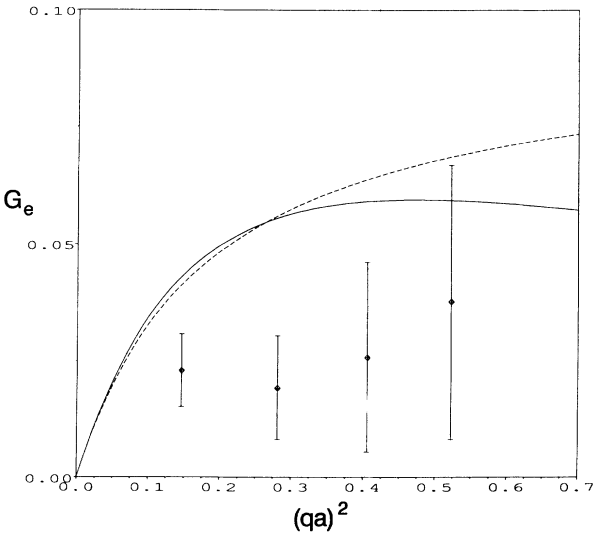

FIG. 8. Same as Fig. 7, except at $\kappa=0.152$.

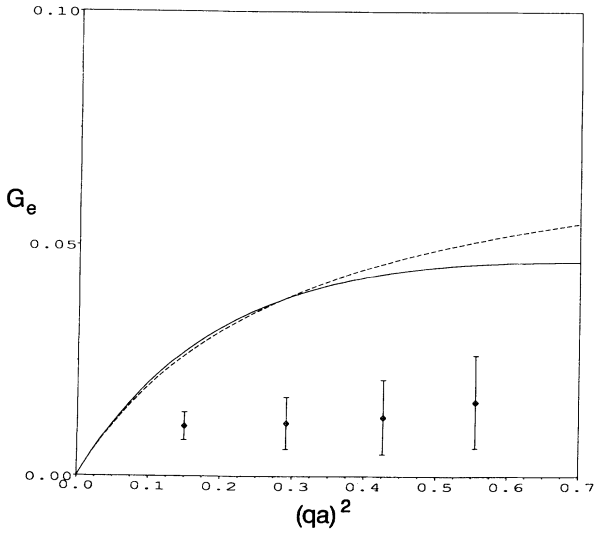

FIG. 9. Same as Fig. 7, except at $\kappa=0.148$.

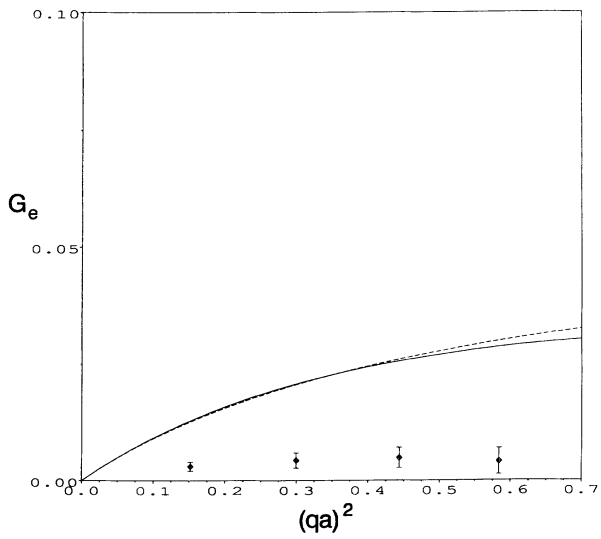

FIG. 10. Same as Fig. 7, except at $\kappa=0.140$.

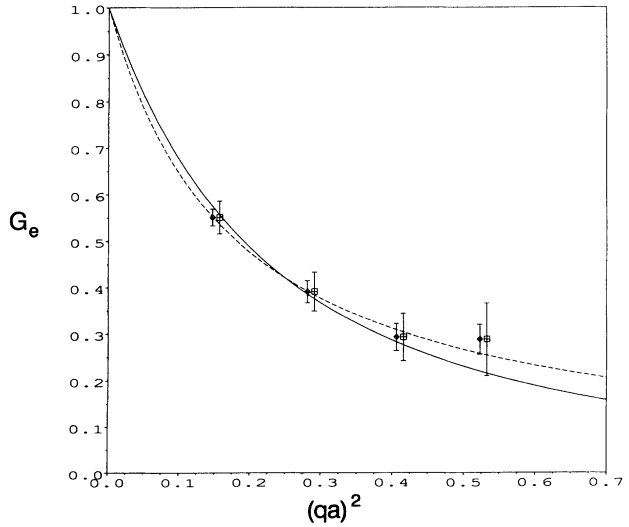

FIG. 11. A comparison at $\kappa=0.152$ of the proton electric form factors calculated by averaging all equivalent momentum transfers (◇) and by not averaging (□). The solid and broken lines represent the best dipole and monopole fits of the proton electric factor, respectively, from Table VII.

TABLE VII. Dipole and monopole fits of the proton electric form factor.

		$\kappa=0.154$	0.152	0.148	0.140
Dipole	$m_D a$	0.593(32)	0.679(20)	0.832(16)	1.12(3)
	R_p/a	5.84(32)	5.10(15)	4.16(8)	3.09(8)
	m_D/m_N	0.801(61)	0.799(30)	0.743(16)	0.688(19)
	χ^2_d	0.25	2.24	1.97	0.41
Monopole	$m_M a$	0.359(31)	0.426(18)	0.542(16)	0.744(23)
	R_p/a	6.82(59)	5.75(24)	4.52(13)	3.29(10)
	m_M/m_N	0.485(49)	0.501(25)	0.484(15)	0.459(15)
	χ^2_d	0.30	0.41	0.42	0.49

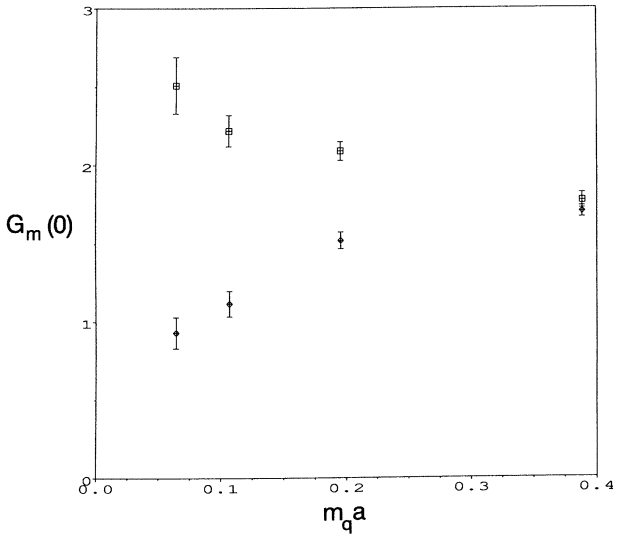

FIG. 12. The magnetic moment of the proton at four values of m_q, which is defined by Eq. (71). The values from the simultaneous fits given in Table VI (□) are contrasted with the extracted values from Eq. (70) (◇).

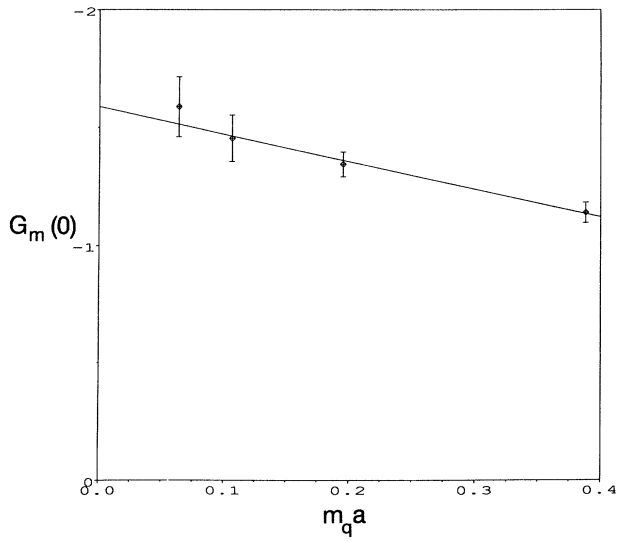

FIG. 14. Linear chiral extrapolation in m_q of the neutron magnetic moment from the simultaneous fits of Table VI.

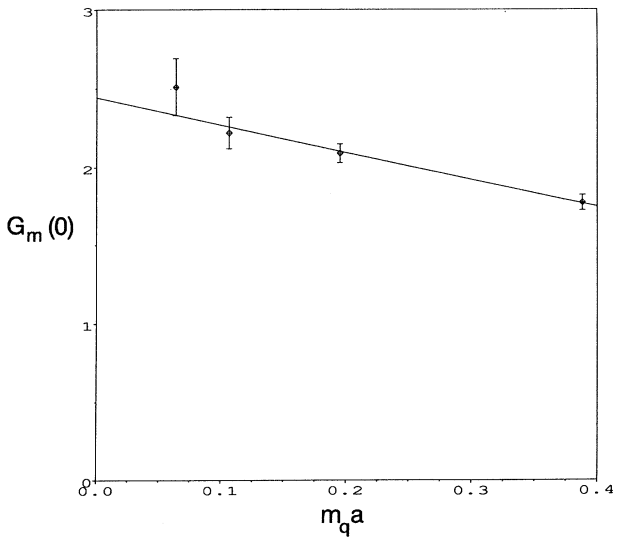

FIG. 13. Linear chiral extrapolation in m_q of the proton magnetic moment from the simultaneous fits of Table VI.

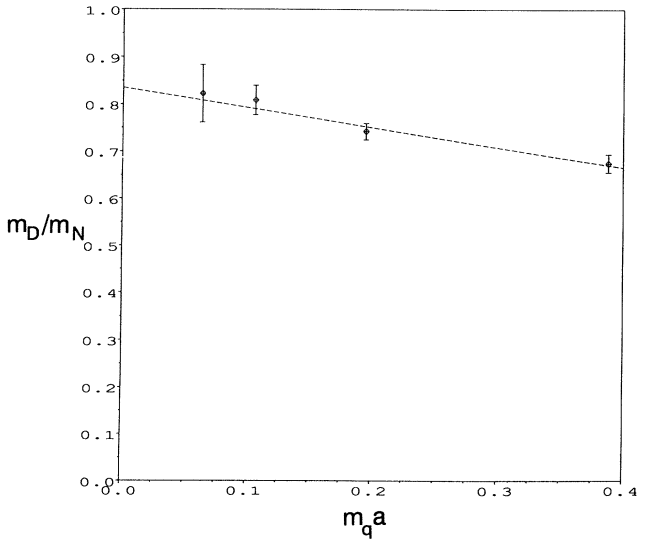

FIG. 15. Linear chiral extrapolation in m_q of the dipole-to-nucleon mass ratio from the simultaneous fits of Table VI.

TABLE VIII. Chiral extrapolation of the proton, neutron magnetic moments, and the mass ratios from Table VI. The experimental data is from Tables X and XI.

		Value	χ^2_d	Experimental fit
Dipole	m_D/m_N	0.836(31)	0.39	0.900(5)
	$G_m^p(0)$	2.44(11)	0.64	2.87(4)
	$G_m^n(0)$	−1.59(11)	0.23	−2.02(5)
Monopole	m_M/m_N	0.516(31)	0.06	0.448(4)
	$G_m^p(0)$	2.48(10)	0.81	3.22(6)
	$G_m^n(0)$	−1.59(12)	0.51	−2.33(6)

tities are encouraging and that the magnetic moments as well as the dipole-to-nucleon mass ratio are reproduced to within about 15%, similar to spectrum calculations. We have also seen an indication that the chiral limit proton and neutron magnetic form factors have a slower falloff in q^2 than the proton electric form factor, which is similar to experiment in this energy regime. In addition, the neutron electric form factors come out to be positive, but their values are poorly represented by a popular phenomenological form at intermediate to small κ values. Finally, we have investigated a zero-momentum technique for extracting magnetic moments, but found that this method yields unrealistically small values as κ_{cr} is approached.

In agreement with the results of Ref. [5], which used $12^2\times24^2$ lattices at $\beta=5.9$, we have found that the magnitudes of the proton and neutron magnetic moments are small compared to experiment, and, indeed, that the neutron value is more badly represented than the proton. The small improvement over the Ref. [5] values could be due to the larger β value used here. Alternatively, we have seen a hint in Figs. 13 and 14 that perhaps better values simply await a closer approach to κ_{cr} rather than requiring larger β values. Another, more interesting, possibility is the unknown contribution to the magnetic moments from disconnected quark loops due to current self-contractions [23]. The Ref. [5] calculation also gave positive values for the neutron electric form factor as was found here. There does seem to be a difference in the physical size of the nucleons in these two studies, however. Corresponding to the dipole and monopole chiral extrapolations in Table IX, we find that the dimensionless quantity $R_p m_N$ has a value 4.23(18) from the dipole fit and a value 4.80(35) from the monopole fit. If we simply divide these results by the experimental (average) nucleon mass, equivalent to the procedure adopted in Ref. [5], we then obtain a charge radius of 0.89 (4) fm from the dipole fit and 1.01(7)fm from the monopole fit as compared to the estimate 0.65(8) fm from Ref. [5]. The experimental result is 0.862(12) fm [24]. The Ref. [5] result corresponds to a dipole-to-nucleon mass ratio which is larger

TABLE IX. Chiral extrapolation of the dipole and monopole proton mass ratios from Table VII.

	Value	χ^2_d	Experimental fit
m_D/m_N	0.818(35)	0.31	0.883(6)
m_M/m_N	0.510(37)	0.08	0.472(4)

TABLE X. Experimental data for the proton from Ref. [20].

q^2 [(GeV/c)^2]	$G_e(q^2)$	$G_m(q^2)$
0.65	0.265(12)	0.767(8)
0.72	0.270(17)	0.690(10)
0.78	0.217(7)	0.647(6)
0.94	0.196(8)	0.523(6)
1.1	0.141(5)	0.452(4)
1.35	0.114(5)	0.352(3)
1.75	0.0713(64)	0.248(3)

than the experimental result by about 25%, whereas the result here is about 7% low compared to experiment. It is unlikely that the physical box size plays an important role in this difference since, assuming renormalization group scaling, the box dimensions of these two calculations are very close (comparing with the shortest box dimension of Ref. [5]). The systematics associated with the different techniques of extracting the form factors could be responsible for these rather different results.

Recent studies of scaling show that both the dimensionless ratios of the string tension [25] and the scalar glueball mass to the chiral condensate [26] have scaling violations of ~20% from $\beta=5.7$ to $\beta=5.9$ and ~10% from $\beta=5.9$ to $\beta=6.0$. Although glueball mass studies on large lattices seem to show scaling from $\beta=5.9$ to $\beta=6.2$ [27], hadron masses and f_π ratios still show a deviation of the order of ~10 to 20% [28]. Therefore, masses and magnetic moments measured at $\beta=6.0$ are subject to a scale-breaking systematic error which could be as large as ~20%, although our use of mass ratios in the monopole and dipole fits would be expected to significantly reduce the systematic error in the extrapolation of the functional forms to the chiral limit.

The overall message of form-factor measurements to this point seems to be that the quenched approximation adequately represents the bulk of the physics of these quantities; however, we are still far from being able to *test* QCD in a precise experimental way on the lattice. At the same time, we should keep in mind that another major theme of such calculations is the increased physics understanding that will be afforded through increasingly sophisticated parametrizations of lattice laboratory data. This has the potential of teaching us about the dynamics associated with quark masses, current self-contraction graphs, and the quenched approximation. It is clear that significantly larger computer resources will be necessary to make substantial progress in our understanding of

TABLE XI. Experimental data for the neutron from Ref. [21].

q^2 [(GeV/c)^2]	$G_m(q^2)$
0.60	−0.629(20)
0.78	−0.434(23)
1.0	−0.345(27)
1.0	−0.322(18)
1.17	−0.284(26)
1.53	−0.203(11)
1.80	−0.185(17)

these issues; we therefore look forward to the benefits of improvements in computer technology, such as proposed in Ref. [29].

ACKNOWLEDGMENTS

This research was supported in part by DOE Grant No. DE-FG05-84ER40154 as well as NSF Grant No. STI-9108764. The calculations were done on the Cray 2 computers at the National Energy Research Computer Center. W.W. would like to thank the Baylor Summer Sabbatical Program for past support. We are also very grateful to Dwight E. Neuenschwander and Chi-Min Wu for assistance with the work described here and to Weiqiang Liu for providing a copy of his Coulomb gauge-fixing program.

[1] T. Draper, R. M. Woloshyn, W. Wilcox, and K. F. Liu, Nucl. Phys. **B318**, 319 (1989).

[2] K. F. Liu, J. M. Wu, S. J. Dong, and W. Wilcox, in *Lattice '90,* Proceedings of the International Conference on Lattice field Theory, Tallahassee, Florida, 1990, edited by U. M. Heller, A. D. Kennedy, and S. Sanielevici [Nucl. Phys. B (Proc. Suppl.) **20**, 467 (1990)]; K. F. Liu, S. J. Dong, and W. Wilcox (unpublished).

[3] G. Martinelli and C. T. Sachrajda, Nucl. Phys. **B316**, 355 (1989).

[4] T. Draper, R. M. Woloshyn, and K. F. Liu, Phys. Lett. B **234**, 121 (1990).

[5] D. B. Leinweber, R. M. Woloshyn, and T. Draper, Phys. Rev. D **43**, 1659 (1991).

[6] T. Draper, R. M. Woloshyn, W. Wilcox, and K. F. Liu, in *Lattice '88,* Proceedings of the Symposium on Lattice Field Theory, Batavia, Illinois, 1988, edited by A. S. Kronfeld and P. B. Mackenzie [Nucl. Phys. B (Proc. Suppl.) **9**, 175 (1989)]. Beware of the different normalization of the conserved current relative to the present paper.

[7] W. Wilcox, K. F. Liu, T. Draper, and C. M. Wu, in *Lattice '89,* Proceedings of the Symposium on Lattice Field Theory, Capri, Italy, 1989, edited by R. Petronzio *et al.* [Nucl. Phys. B (Proc. Suppl.) **17**, 382 (1990)].

[8] J. J. Sakurai, *Advanced Quantum Mechanics* (Addision-Wesley, Reading, PA, 1967).

[9] L. H. Karsten and J. Smit, Nucl. Phys. **B183**, 103 (1981).

[10] D. Soper, Phys. Rev. D **18**, 4590 (1978).

[11] We require the correspondence $e^{iS_F^M[\bar{\psi},\psi]} \rightarrow e^{-S_F^E[\bar{\zeta},\zeta]}$ under $t \rightarrow -it$, which identifies $S_F^E[\bar{\zeta},\zeta]$ as $S_F^E[\bar{\zeta},\zeta] = \sum_{I,J} \bar{\zeta}_I M_{IJ}[U^\dagger]\zeta_J$, where $U_\mu^\dagger$ is now the usual Euclidean link variable.

[12] C. Bernard, T. Draper, G. Hockney, and A. Soni, in *Lattice Gauge Theory: A Challenge in Large-Scale Computing,* Proceedings of the Workshop, Wuppertal, Germany, 1985, edited by B. Bunk, K. H. Mutter, and K. Schilling, NATO Advanced Study Institute, Series B: Physics, Vol. 140 (Plenum, New York, 1986); C. Bernard, in *Gauge Theory on a Lattice,* edited by C. Zachos, W. Celmaster, E. Kovacs, and D. Sivers (National Technical Information Service, Springfield, VA, 1984), p. 85.

[13] N. Cabibbo and E. Marinari, Phys. Lett. **119B**, 387 (1982).

[14] R. Gupta, G. Guralnik, G. Kilcup, A. Patel, S. Sharpe, and T. Warnock, Phys. Rev. D **36**, 2813 (1987).

[15] C. Bernard, A. El-Khadra, and A. Soni, Phys. Rev. D **43**, 2140 (1991).

[16] T. A. DeGrand, Comput. Phys. Commun. **52**, 161 (1988).

[17] P. Bacilieri *et al.*, Phys. Lett. B **214**, 115 (1988).

[18] S. Cabasino *et al.*, in *Lattice '90* [2], p. 399.

[19] W. Wilcox, Phys. Rev. D **43**, 2443 (1991).

[20] L. E. Price, Phys. Rev. D **4**, 45 (1975).

[21] W. Bartel *et al.*, Nucl. Phys. **B58**, 429 (1973). Note that we have supplied the known value of the neutron's magnetic moment to extract form factor data from Table VIII of this reference.

[22] M. Gourdin, Phys. Rep. **11C**, 1 (1974).

[23] D. B. Leinweber, Phys. Rev. D **45**, 252 (1992).

[24] G. G. Simon *et al.*, Z. Naturforsch. **35a**, 1 (1980).

[25] G. Salina and A. Vladikas, in *Lattice '90* [2], p. 181.

[26] G. Schierholz, in *Lattice '88* [6], p. 244; P. Bacilieri *et al.*, Phys. Lett. B **205**, 535 (1988).

[27] C. Michael and M. Teper, Nucl. Phys. **B314**, 347 (1989).

[28] R. Gupta, G. Guralnik, G. Kilcup, and S. Sharpe, Phys. Rev. D **43**, 2003 (1991).

[29] QCD Teraflop Collaboration, Int. J. Mod. Phys. C **2**, 829 (1991).